Chinese Chemical Letters 37 (2026) 111457

Contents lists available at ScienceDirect

Chinese Chemical Letters

journal homepage: www.elsevier.com/locate/cclet

# Interfacial engineering of $ZnIn_2S_4$@$AgBiS_2$ high-low heterojunction for boosted photocatalytic $H_2$ evolution

Xueting Liu[a], Wei Li[b,*], Zheng Liu[a], Yuemin Wang[a], Rui Xiong[a], Pengfei Fang[a], Chunxu Pan[a], Jianhong Wei[a,*]

[a] Key Laboratory of Artificial Micro- and Nano-structures of Ministry of Education, and School of Physics and Technology, Wuhan University, Wuhan 430072, China

[b] School of Materials and Environmental Engineering, Chengdu Technological University, Chengdu 610031, China

ARTICLE INFO

*Article history:*
Received 24 April 2025
Revised 11 June 2025
Accepted 13 June 2025
Available online 13 June 2025

*Keywords:*
Transition metal sulfide
Charge carrier dynamics
DFT calculation
S-scheme heterojunction
Photocatalytic $H_2$ evolution

ABSTRACT

The sluggish dynamics of photogenerated carriers and low sunlight absorption rate severely impede the performance of $ZnIn_2S_4$-based photocatalysts. To enhance their photoactivity, Sv-$ZnIn_2S_4$@$AgBiS_2$ (Sv-ZIS@ABS) heterostructure composites with sulfur-rich vacancies were synthesized by growing $ZnIn_2S_4$ nanosheets on the surface of $AgBiS_2$ through a one-step solvothermal method. The results demonstrate that the Sv-ZIS@ABS composites possess a substantially larger specific surface area and remarkable photocatalytic performance, achieving a hydrogen evolution rate of 4560.2 μmol $h^{-1}$ $g^{-1}$, approximately 14.27 times higher than that of pristine ZIS. The electron transfer kinetics in the ZIS@ABS heterojunction were thoroughly investigated using photoluminescence (PL), charge differential density, kelvin probe force microscope (KPFM), and *in situ* XPS, *etc*. Based on photocatalytic $H_2$ evolution experiments and density functional theory (DFT) calculations, a plausible photocatalytic mechanism for the Sv-ZIS@ABS composites was proposed. This study provides valuable insights into the design of highly efficient transition metal sulfide-based heterojunction photocatalysts, with a focus on optimizing electron transfer kinetics in these semiconductor materials.

© 2026 Published by Elsevier B.V. on behalf of Chinese Chemical Society and Institute of Materia Medica, Chinese Academy of Medical Sciences.

Since the emergence of photocatalytic technology in the 1970s, numerous photocatalytic materials have been developed and their mechanisms extensively studied due to the technology's green, non-polluting, and sustainable characteristics. However, early photocatalytic materials, primarily $TiO_2$, exhibited limited photocatalytic applications because of their wide band gaps, leading to inefficient utilization of sunlight. Consequently, developing new photocatalytic materials with the ability of absorbing visible or infrared light is of significant importance. To date, extensive research has been conducted on various types of semiconductor photocatalytic materials, such as metal oxides [1], metal sulfides [2], metal phosphide [3], perovskite materials [4], and metal-organic frameworks (MOFs) or MOF derivation [5,6]. Among these materials, transition metal sulfides, such as $ZnIn_2S_4$ (ZIS), $MnIn_2S_4$, have garnered increasing attention for its adjustable band gap, suitable band edge positions, exceptional photoelectric properties, and cost-effectiveness [7,8]. Nonetheless, the poor light absorption capacity, and low quantum yield severely impeding its further advancement.

Currently, extensive efforts have been made to address these issues through approaches such as morphology control, defect engineering, and heterojunction formation. Recently, Zhang *et al.* prepared a ternary C/CdS@ZIS photocatalyst by anchoring CdS nanoparticles onto a hollow carbon scaffold and subsequently encapsulating it with a ZIS outer layer. This unique hollow structure not only enhances light absorption but also provides an extensive surface area for $CO_2$ adsorption, leading to a notable CO yield of 115.4 μmol $h^{-1}$ $g^{-1}$, which is 53.2 times higher than pristine CdS samplesand 7 times greater than bare ZIS [9]. Similarly, Du *et al.* introduced sulfur vacancies and constructed heterojunctions to synthesize hollow $TiO_2$@ZIS composites. These composites feature abundant active sites and improved light-harvesting capabilities, which facilitate efficient charge separation. Correspondingly, the $CO_2$ photoreduction activity was significantly boosted, achieving a CO production rate of 1330 μmol $g^{-1}$ $h^{-1}$, surpassing that of pure ZIS (639 μmol $g^{-1}$ $h^{-1}$) by two-fold [10]. These findings underscore the effectiveness of these strategies in enhancing the performance of metal sulfide-based photocatalytic materials.

Conversely, bismuth-based nanomaterials have attracted considerable interest because of their distinctive electronic band struc-

* Corresponding authors.
*E-mail addresses:* wli2014@whu.edu.cn (W. Li), jhwei@whu.edu.cn (J. Wei).

https://doi.org/10.1016/j.cclet.2025.111457
1001-8417/© 2026 Published by Elsevier B.V. on behalf of Chinese Chemical Society and Institute of Materia Medica, Chinese Academy of Medical Sciences.

tures, superior photoelectric characteristics, and morphological tunability. Such as, $AgBiS_2$ (ABS), a representative ternary bismuth sulfide, exhibits notable light absorption across the UV–vis-NIR spectrum and generates robust photoelectrochemical responses when stimulated with 980-nm light, has been extensive applications in thin film solar cells, ion batteries and photocatalytic degradation of pollutants [11,12]. Besides, it is also an ideal cocatalyst by providing additional active sites and regulating the electronic density of the catalyst. Meanwhile, the co-shared S atoms are conducive to reducing the charge transfer resistance [13]. In this study, flower-like Sv-ZIS@ABS heterojunction composites were synthesized through the *in situ* formation of sulfur vacancies-modified ZIS nanosheets (Sv-ZIS) on ABS nanoflowers. Various methods were employed to assess the sturcture and photoelectric properties of the as-prepared samples. The photocatalytic activity of Sv-ZIS@ABS was evaluated through hydrogen production experiments, and a plausible photo-reactivity mechanism was proposed.

The typical preparation process for the Sv-ZIS@ABS heterojunction is described as follows: Initially, flower-like $AgBiS_2$ samples are synthesized *via* a solvothermal approach. Next, $Zn^{2+}$ and $In^{3+}$ ions are readily adsorbed onto the surface of $AgBiS_2$ through electrostatic self-assembly interactions. Following this, the adsorbed $Zn^{2+}$ and $In^{3+}$ ions react with $S^{2-}$ ions from the added thioacetamide (TAA), leading to the *in-situ* formation of Sv-ZIS on the $AgBiS_2$ surface and the construction of tightly integrated Sv-ZIS@ABS heterojunctions. The co-share sulfur element enhances the adhesion between Sv-ZIS and the $AgBiS_2$ substrate. For a detailed description of the preparation process, refer to the supporting information.

The design and synthesis of the Sv-ZIS@ABS heterojunction is shown in Fig. 1a. Briefly, flower-like $AgBiS_2$ were first formed using solvothermal method. Subsequently, Sv-ZIS was *in-situ* generated onto $AgBiS_2$ surfaces to form Sv-ZIS@ABS nanocomposite by low temperature oil bath method. The co-share S element enhance the adhesion of the Sv-ZIS on the ABS substrate surface. The morphology, composition, and structure of various samples were analyzed using scanning electron microscopy (SEM), transmission electron microscopy (TEM), high-resolution transmission electron microscopy (HRTEM), and elemental mappings (Figs. 1b-h). It was observed that the pristine ABS exhibited a flower-like structure comprising smooth stacked nanosheets with a lateral diameter of 0.5 μm and thickness of 50 nm (Fig. 1b).

The pristine Sv-ZIS samples were microsphere structure composed of many nanosheets with diameter about several microns (Fig. 1c). Fig. 1d demonstrated that the Sv-ZIS@ABS-2 samples possessed a loose, cauliflower-like morphology. The TEM image of the Sv-ZIS@ABS-2 samples (Fig. 1e) further validated this flower-like structure, with 2D Sv-ZIS nanosheets firmly adhering to the ABS surface. The HRTEM images (Fig. 1f) distinctly revealed lattice fringes measuring 0.28 nm and 0.32 nm, which correspond to the ABS (200) and Sv-ZIS (102) crystal planes, respectively. In addition, discontinuous lattice streaks (marked with yellow circles in Fig. 1g) indicate the presence of sulfur vacancies in the Sv-ZIS@ABS-2 heterojunction photocatalyst [14]. Defects play a crucial role in adjusting the electronic structure and act as efficient trapping centers for photoinduced charge carriers, thereby demonstrating substantial importance in photocatalytic applications. The element mapping in the Fig. 1h displayed the uneven distribution of Ag, Bi, S, In and Zn elements in the Sv-ZIS@ABS-2 composites, inferring Sv-ZIS have been successfully coupled onto the ABS surface during the low-temperature oil bath process.

The XRD analysis was performed to examine the crystalline structure of the synthesized samples, as presented in Fig. 2a. By comparing with the standard PDF card of $ZnIn_2S_4$ (ZIS), it was observed that the characteristic peak positions of Sv-ZIS samples exhibited close alignment with hexagonal ZIS (JCPDS No. 65–2023). The diffraction peaks observed at 21.1°, 27.5°, 47.2°, 52.2°, and 55.6° can be attributed to the (006), (102), (110), (116), and (022) crystallographic planes of hexagonal $ZnIn_2S_4$ [15,16]. No impurity peaks were detected in the as-prepared Sv-ZIS samples, suggesting that sulfur vacancies have a negligible effect on its crystallinity. The diffraction peaks observed at 27.3°, 31.7°, 45.4°, 53.8°, 56.4°, and 66.1° in the $AgBiS_2$ (ABS) pattern correspond to the (111), (200), (220), (311), (222), and (400) crystallographic planes of cubic

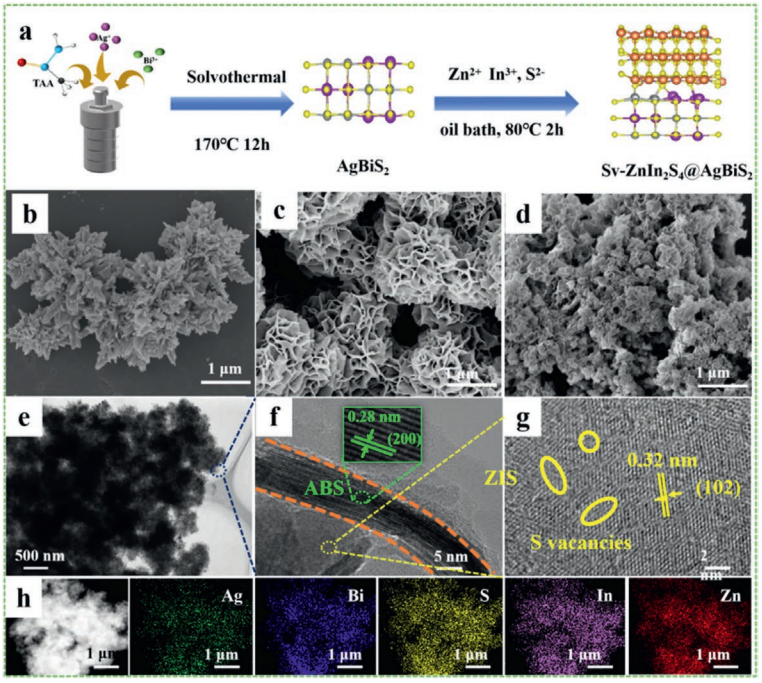



**Fig. 1.** (a) Schematic illustration of Sv-ZIS@ABS heterojunction. SEM images of (b) ABS, (c) Sv-ZIS and (d) Sv-ZIS@ABS-2. (e) TEM, (f, g) HRTEM images and (h) elemental mappings of Sv-ZIS@ABS-2.

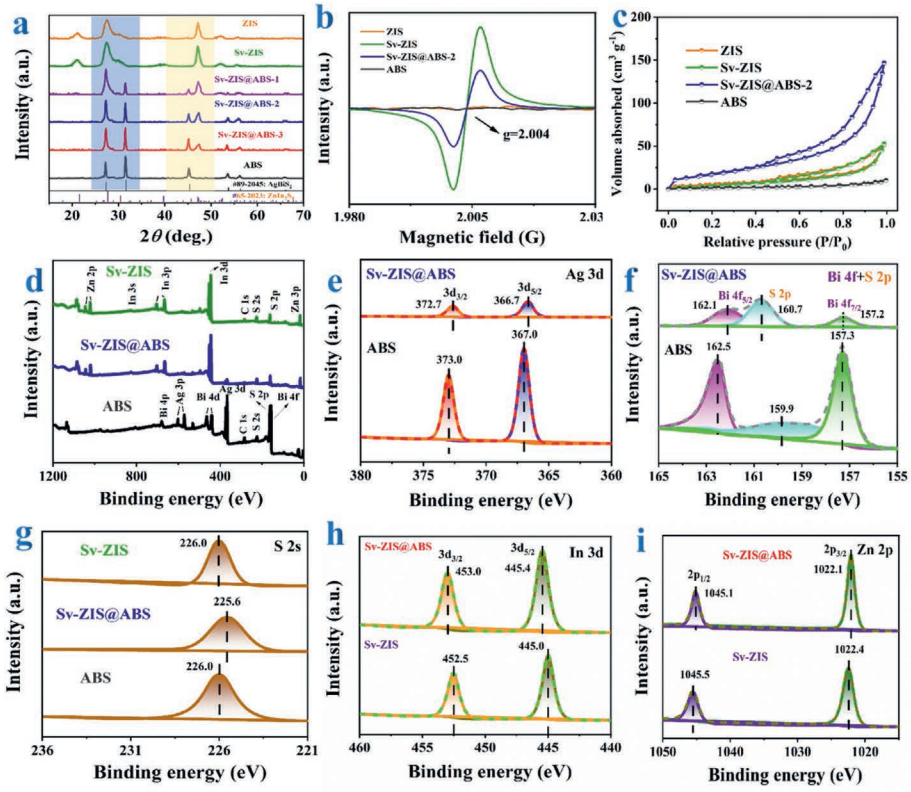



**Fig. 2.** (a) XRD patterns of the as-prepared samples. (b) ESR spectra. (c) BET high-resolution. XPS spectra of (d) survey, (e) Ag 3d, (f) Bi 4f+S 2p, (g) S 2s, (h) In 3d and (i) Zn 2p for ZIS, Sv-ZIS, Sv-ZIS@ABS and ABS.

ABS, respectively, as confirmed by reference to JCPDS No. 89–2045 [17,18]. The XRD spectra of Sv-ZIS@ABS composites display characteristic diffraction peaks from both components. As the proportion of ABS increases, the peaks corresponding to Sv-ZIS gradually diminish, whereas the characteristic peaks attributed to ABS become more pronounced. These observations provide additional evidence for the simultaneous presence of Sv-ZIS and ABS within the composite material system.

Fig. 2b exhibits the electron spin resonance (ESR) spectra of the as-prepared samples. A sharper peak located at $g = 2.004$ in the ESR spectra indicates the presence of sulfur vacancies in Sv-ZIS and Sv-ZIS@ABS-2 [19]. However, the signal intensity for Sv-ZIS was significantly stronger than that of Sv-ZIS@ABS-2, meanwhile, no distinct peaks were observed near $g = 2.004$ for the pure Sv-ZIS and ABS samples. These findings confirm the successful introduction of sulfur vacancies into Sv-ZIS and Sv-ZIS@ABS-2.

The specific surface areas ($S_{BET}$) was investigated by $N_2$ adsorption/desorption isotherms (Fig. 2c). According to the Barrett-Joyner-Halenda (BJH) analysis, the $S_{BET}$ of ZIS, Sv-ZIS, ABS, and Sv-ZIS@ABS-2 are 26.9, 28.1, 59.3 and 113.1 $m^2/g$, respectively (Table S1 in Supporting information). Notably, the $S_{BET}$ of Sv-ZIS@ABS-2 is much higher than that of corresponding monomer, which infers that the suitable addition of Sv-ZIS is beneficial for improving the adsorption performance and photocatalytic performance. Fig. 2d indicated high-resolution XPS spectra of as-prepared samples. The XPS survey spectrum of Sv-ZIS@ABS confirms the presence of Zn, In, S, Ag, Bi, and C elements. Specifically, the characteristic peaks for Zn, In, and S are indicative of the Sv-ZIS nanosheets, whereas the signals for Ag, Bi, and S are associated with the $AgBiS_2$ nanoparticles. The detected C signal is likely due to adsorbed solvent molecules. The high-resolution Ag 3d spectrum displays two prominent peaks at 367 eV (Ag $3d_{5/2}$) and 373 eV (Ag $3d_{3/2}$), which align with previously reported values for $Ag^+$ ions [20]. Compared with ABS samples, the above two Ag 3d signals negatively transfer to 366.7 and 372.7 eV, respectively in Sv-ZIS@ABS sample (Fig. 2e), confirming that the electron density around Ag atom increased after ABS samples were combined with Sv-ZIS samples [21,22]. Since the characteristic peaks of Bi 4f and S 2p were located relatively close to each other, they were both represented in Fig. 2f. For Bi 4f, the two characteristic peaks of Bi $4f_{7/2}$ and Bi $4f_{5/2}$ in Sv-ZIS@ABS composite located at 157.2 and 162.1 eV, while those of them in ABS samples located at 157.3 and 162.5 eV, respectively [23,24]. Besides, a little peak located at 160.7 eV in ABS can be ascribed to S 2p electrons, which transfer to 159.9 eV in the composites. In Fig. 2g, it is observed that the characteristic peaks of S 2s for Sv-ZIS and ABS both were located at 226.0 eV, agreeing well with that of $S_2^-$ [25]. In contrast, the S 2s signals in the Sv-ZIS@ABS composites exhibit a negative shift compared to those of the corresponding monomer, suggesting a strongly interacting process existence between Sv-ZIS and ABS. Additionally, the characteristic peaks of In 3d (445.0 and 452.5 eV) and Zn 2p (1022.1 and 1045.1 eV) in the Sv-ZIS samples exhibit a negative shift of approximately 0.3–0.5 eV in the Sv-ZIS@ABS composite (Figs. 2h and i). These observations suggest that charge transfer occurs at the interface between Sv-ZIS and ABS in the Sv-ZIS@ABS composites [26,27].

The optoelectric properties of diverse samples were analyzed using UV-visible diffuse reflectance spectroscopy (UV–vis DRS), as depicted in Fig. 3a. The absorption characteristics of pristine ZIS nanosheets were essentially identical to those of Sv-ZIS samples, with both exhibiting an absorption edge around 550 nm, while the absorption edge of ABS samples was observed in the near-infrared (near-IR) region. For the Sv-ZIS@ABS composite samples, the light absorption capability of the prepared materials progressively enhanced as the ABS content increased. Based on Tauc's equation, the calculated bandgap values were 2.27, 2.25, 2.17, 2.06, 1.87 and

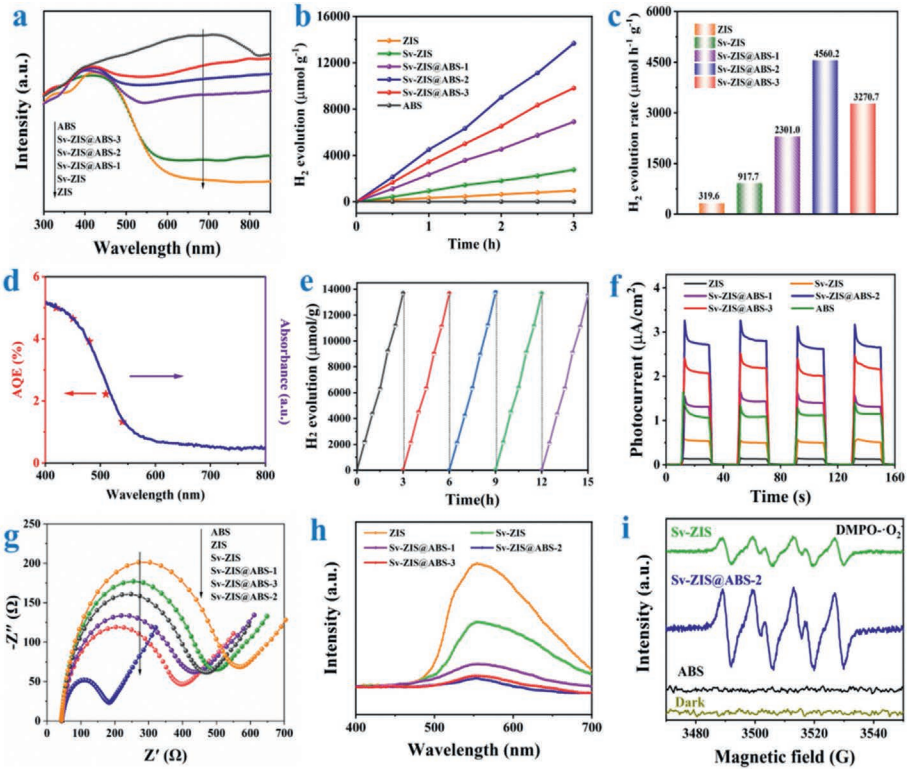



**Fig. 3.** (a) UV–vis DRS, and (b, c) comparison of photocatalytic $H_2$ evolution for different samples. (d) UV–vis DRS (blue line) and wavelength dependence apparent quantum efficiency (AQE) (red dots) of Sv-ZIS@ABS-2. (e) $H_2$ evolution stability for Sv-ZIS@ABS-2 samples. (f) *I-t* response curves and (g) EIS spectra, (h) PL, (i) ESR spectra of $\cdot O_2^-$ under visible light irradiation of various samples.

1.25 eV for ZIS, Sv-ZIS, Sv-ZIS@ABS-1, Sv-ZIS@ABS-2, Sv-ZIS@ABS-3 and ABS samples, respectively (Fig. S1 in Supporting information). Figs. S2a and b (Supporting information) displayed the Mott-Shottky (MS) plots of Sv-ZIS and ABS samples, both of them exhibit positive slopes, corresponding to N-type semiconductor. The flat band potentials ($E_{fb}$) for Sv-ZIS and ABS were determined to be −1.00 V and −0.30 V (*vs.* Ag/AgCl), respectively, reflecting their conduction band (CB) potentials [28]. Using the bandgap values shown in Fig. S1 and applying the formula $E_g = E_{vb} - E_{cb}$, the valence band (VB) positions of Sv-ZIS and ABS were calculated to be 1.25 V and 0.95 V, respectively [29,30]. By evaluating these parameters, we can infer that the conduction and valence band positions for Sv-ZIS are −1.00 V and 1.25 V, while for ABS, they are −0.30 V and 0.95 V, respectively.

The photocatalytic performance of the synthesized samples was evaluated through hydrogen generation under visible light irradiation ($\lambda > 420$ nm). As depicted (Figs. 3b and c), the pure ABS sample demonstrated minimal hydrogen evolution because of sereve electron-hole recombination caused by the relatively narrow bandgap or insufficient reducibility of electrons at the conduction band position, while the pure ZIS and Sv-ZIS samples displayed photocatalytic $H_2$ evolution (PHE) amount of 958.8 and 2751.3 μmol/g at 3 h, respectively. For Sv-ZIS-modified ABS samples, the PHE rate initially increases and subsequently decreases as the Sv-ZIS content rises, suggesting that an insufficient amount of Sv-ZIS nanosheets lead to a lack of active substances necessary for the photocatalytic reaction. Conversely, an excessive number of Sv-ZIS nanosheets on the composite surface hinder light absorption by the inner layers of the ABS samples. Obviously, the PHE performance of Sv-ZIS@ABS composites was markedly superior to that of pristine ZIS and Sv-ZIS samples. Notably, the Sv-ZIS@ABS-2 sample exhibited maximum PHE rate of 4560.2 μmol $h^{-1}$ $g^{-1}$, representing a 14.27- and 4.97-fold increase over pure ZIS and Sv-ZIS samples, respectively. This substantial enhancement maybe attributed to the formation of heterojunction at the interface of Sv-ZIS and ABS, which greatly promoted the separation and transfer of photogenerated charges. On the other hand, the sulfur vacancies as the electron capture centers in Sv-ZIS further suppressed the recombination of electron-hole pairs. Moreover, the special loose porous core-shell structure of Sv-ZIS@ABS composites was beneficial for absorbing more photons to participating in photochemical reaction, thus exhibiting significant boosted photocatalytic $H_2$ evolution performance [31–33]. Furthermore, the PHE performance of the Sv-ZIS@ABS-2 sample prepared by physical mixing is much lower than that of the Sv-ZIS@ABS-2 sample prepared by solvothermal method (Fig. S3 in Supporting information), confirming the successful construction of the Sv-ZIS@ABS heterojunction. Notably, the Sv-ZIS@ABS-2 exhibits an apparent quantum efficiency (AQE) of 5.05 %, 4.71 %, 4.11 %, 2.25 % and 1.36 % at 420, 450, 480, 510 and 540 nm, respectively (Fig. 3d). This rule was consistent with the trend shown by the UV–vis spectra of pristine Sv-ZIS nanosheets, indicating that the photocatalytic $H_2$ evolution process of Sv-ZIS@ABS-2 composite samples was indeed excited by visible light. It could be observed that the total $H_2$ evolution for Sv-ZIS@ABS-2 during 5 cycles cycle has little change (Fig. 3e). Meanwhile, the XRD patterns and XPS spectra of Sv-ZIS@ABS-2 before and after the hydrogen evolution reaction (Fig. S4 in Supporting information) did not exhibit obvious changes, revealing its excellent photocatalytic stability.

To better understand photocatalytic $H_2$ evolution mechanism, a series of photo/electrochemical measurements were performed. As shown in Fig. 3f, the photocurrent produced by Sv-ZIS@ABS composites significantly outperformed that of the unmodified samples. Specifically, the optimal sample (Sv-ZIS@ABS-2) generated a photocurrent of 3.26 μA/cm², which is approximately 20.96, 5.18, and 2.59 times higher than that of ZIS, Sv-ZIS, and ABS, respec-

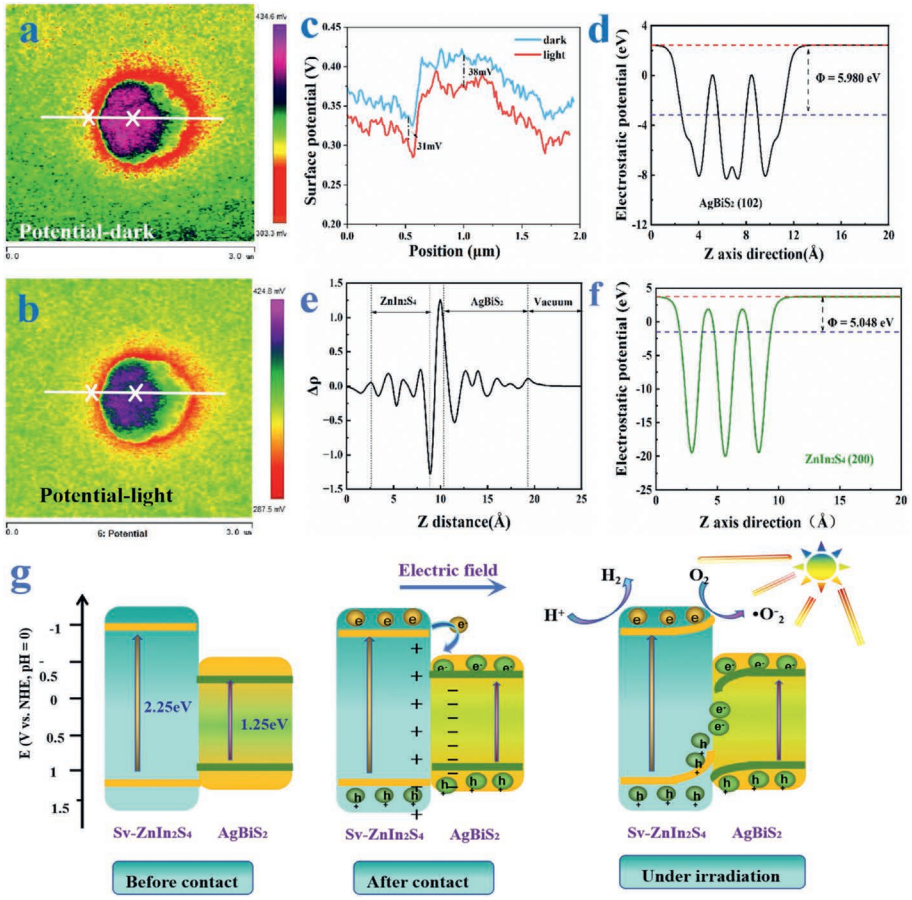



**Fig. 4.** (a) KPFM images of Sv-ZIS@ABS-2 in dark. (b) KPFM image of Sv-ZIS@ABS-2 under light illumination. (c) Corresponding surface potential profiles of Sv-ZIS@ABS-2 in the dark and light illumination. (d) DFT calculated work function for $AgBiS_2$. (e) The charge differential density of Sv-ZIS@ABS composites. (f) DFT calculated work function for Sv-ZIS. (g) The possible photo-reactivity mechanism for Sv-ZIS@ABS composites.

tively. Additionally, the photocurrent densities of the Sv-ZIS@ABS composites followed the order: Sv-ZIS@ABS-2 > Sv-ZIS@ABS-3 > Sv-ZIS@ABS-1. This trend aligns well with the results obtained from photocatalytic $H_2$ evolution activity. Fig. 3g compared the EIS curves of various samples, and the tendency was consistent with the order of photocurrent in Fig. 3f. In addition, compared with the Sv-ZIS (87.23 μF/cm$^2$) and ABS (53.28 μF/cm$^2$), Sv-ZIS@ABS-2 (107.89 μF/cm$^2$) exhibits a larger electrochemical surface area (ECSA, Fig. S5 in Supporting information). The PHE rate per ECSA for Sv-ZIS@ABS is separately 7.2 and 4.1 times larger than those of ABS and Sv-ZIS, again demonstrating that the construction of high-low heterojunction is beneficial to exposed more active sites [34–36], thereby leading to higher PHE activity. In summary, these findings validate improved separation and transfer of photogenerated charge carriers and exposed more active sits in the Sv-ZIS@ABS-2, correspondingly resulting in promoting photocatalytic $H_2$ evolution activity. Additionally, it is observed a noticeable decrease in the photoluminescence (PL) intensity of Sv-ZIS@ABS compared to ZIS, Sv-ZIS and ABS (Fig. 3h). This reduction suggests that charge recombination was effectively suppressed due to enhanced charge separation in the Sv-ZIS@ABS heterostructures. To confirm the photoreactivity mechanism, we conducted ESR analysis (Fig. 3i) with DMPO as the trapping agent to detect superoxide radicals ($^{\bullet}O_2^-$) in an aqueous solution. No signals were observed in dark for all the samples, indicating that $^{\bullet}O_2^-$ generation requires light stimulation. Meantime, no signals was observed for ABS under visible light irradiation, which maybe due to its CB band edge at −0.30 eV, exhibits a limited capability for transferring $O_2$ into $^{\bullet}O_2^-$ . Upon irradiation, the Sv-ZIS@ABS-2 sample exhibited stronger DMPO-$^{\bullet}O_2^-$ signals compared to Sv-ZIS and ABS alone, indicating a more efficient process for converting free electrons and holes into active $^{\bullet}O_2^-$ radicals. The Sv-ZIS@ABS exhibited a significantly stronger $^{\bullet}O_2^-$ signal compared to Sv-ZIS, indicating a possible S-scheme mechanism existence during the photoreaction process.

To achieve a more comprehensive understanding of the kinetic mechanisms, the surface potential of Sv-ZIS@ABS-2 was investigated using *in situ* Kelvin probe force microscopy (KPFM) to gain deeper insights into the charge transfer mechanism occurring between Sv-ZIS and ABS (Fig. 4). Figs. 4a and b display KPFM images of Sv-ZIS@ABS-2 in dark and light conditions, respectively. Fig. 4c exhibits the surface potential distribution of the line profile Sv-ZIS@ABS-2 under dark and light conditions. In Fig. 4c, the surface potential at point A and B decreases by 31 and 38 mV respectively under light illumination compared to dark conditions. Meanwhile, the total surface potentials along the linear profile were decreased under light illumination compared to those in the dark condition. These results indicate that photogenerated electrons are enriched at the Sv-ZIS interface in Sv-ZIS@ABS-2 under photoexcitation [37–39].

To assess the work functions of $AgBiS_2$ and $ZnIn_2S_4$, as well as the charge difference density at their heterojunction interface, density functional theory (DFT) calculations were employed (Figs. 4d-f). The Fermi level ($E_f$) was determined using the formula $E_f = E_{vac}$ - $\Phi$, where $E_{vac}$ denotes the vacuum energy level and $\Phi$ signifies the work function. Compared to Sv-$ZnIn_2S_4$, which has a work function of 5.048 eV, $AgBiS_2$ demonstrates a higher work

function of 5.980 eV, inferring a lower Fermi level. This difference in Fermi levels results in electron transfer from Sv-$ZnIn_2S_4$ to $AgBiS_2$ at the composites interface. This electron transfer persists until the Fermi levels equalize, causing band bending at the interface [40,41]. Additionally, the analysis of differential charge density further confirmed these hypoyhesis. At the interface of $AgBiS_2$ and $ZnIn_2S_4$, there is a noticeable region with varying charge densities. Specifically, an accumulation of electrons is observed on the $AgBiS_2$ side (indicated in yellow), whereas a depletion of electrons occurs on the $ZnIn_2S_4$ side (marked in cyan) (Fig. S6 in Supporting information). Consequently, this distribution creates an internal electric field that points from $ZnIn_2S_4$ toward $AgBiS_2$ (Fig. 4g).

Based on the aforementioned results, the photocatalytic $H_2$ evolution mechanism of the Sv-ZIS@ABS composites was proposed. When exposed to visible light, both Sv-ZIS and ABS undergo electron excitation from their respective valence bands (VB) into their conduction bands (CB), leaving behind holes ($h^+$). Through the influence of Coulomb interactions and built-in electric fields, the photoexcited electrons produced by ABS efficiently pair with holes within Sv-ZIS, leading to the formation of an S-scheme heterojunction [42–45]. This accelerates the charge transfer while maintaining the high reducibility of electrons in the CB of ZIS to take part in photocatalytic $H_2$ evolution reaction (HER), correspondingly result in boosted HER performance.

*In situ* XPS further confirm the electron transfer and the proposed mechanism (Fig. S7 in Supporting information). When compared with the dark conditions, the binding energy values of Zn 2p and In 3d move towards lower values, which implies electron enrichment. Conversely, Ag 3d and Bi 4f show positive shifts, suggesting electron depletion [46]. The electron enrichment and depletion provided strong evidence for the proposed S-scheme heterojunction with photogenerated electrons flowing from ABS to ZIS. This S-scheme charge transfer mechanism significantly enhances the separation efficiency of electron-hole pairs in the Sv-ZIS@ABS composites.

As a result, photogenerated electrons with high reducibility can effectively reduce $H_2O$ to $H_2$ during the photocatalytic hydrogen evolution process. Moreover, the sulfur vacancies in Sv-ZIS not only boost its light absorption ability but also enhance charge transfer efficiency during photocatalysis, thereby improving overall photocatalytic performance. Furthermore, this feature facilitates faster charge transfer while preserving the high reducibility of electrons and the strong oxidation capability of holes, enabling their active participation in photoreactivity. Consequently, the flower-like Sv-ZIS@ABS composite samples, characterized by a large specific surface area, displayed excellent photocatalytic performances under the synergistic action of sulfur vacancies and S-scheme heterojunctions.

In conclusion, flower-like Sv-ZIS@ABS photocatalysts featuring a large specific surface area were successfully synthesized by growing sulfur-vacancy-containing Sv-ZIS ultrathin nanosheets on ABS substrates with a sea urchin-like morphology through a low-temperature oil bath process. The optimal Sv-ZIS@ABS-2 sample exhibited an impressive photocatalytic $H_2$ evolution rate of 4560.2 μmol $h^{-1}$ $g^{-1}$, which is 14.27 and 4.97 times higher than that of ZIS and Sv-ZIS samples, respectively. The synergistic effect of sulfur vacancies and the formation of S-scheme heterojunctions not only promoted the separation efficiency of photogenerated charges, but also inhibited the recombination of electron-hole pairs, thereby markedly improving the photoelectric and photocatalytic performance of Sv-ZIS@ABS photocatalysts. Additionally, the investigation of the electron transfer pathways using KPFM and DFT calculations provided deeper insights into the photocatalytic reaction mechanism of Sv-ZIS@ABS composites with S-scheme heterojunctions.

## CRediT authorship contribution statement

**Xueting Liu:** Writing – original draft, Methodology, Investigation, Data curation. **Wei Li:** Writing – original draft, Supervision, Methodology, Investigation, Data curation. **Zheng Liu:** Validation, Methodology, Investigation. **Yuemin Wang:** Methodology, Investigation, Formal analysis. **Rui Xiong:** Software, Formal analysis, Conceptualization. **Pengfei Fang:** Software, Resources, Investigation. **Chunxu Pan:** Software, Resources, Methodology. **Jianhong Wei:** Writing – review & editing, Supervision, Funding acquisition, Conceptualization.

## Declaration of competing interest

The authors declare that they have no known competing financial interests or personal relationships that could have appeared to influence the work reported in this paper.

## Acknowledgments

This work was supported by National Natural Science Foundation of China (Nos. 12075174 and 91963207), and National Key Research and Development Program of China (No. 2022YFA1602701).

## Supplementary materials

Supplementary material associated with this article can be found, in the online version, at doi:10.1016/j.cclet.2025.111457.

## References

[1] J. Zhang, W.Q. Liao, H. Zheng, et al., J. Catal. 405 (2022) 152–163.
[2] H.R. Zhang, M.Y. Cui, Y.J. Lv, Y.F. Rao, Y. Huang, Chin. Chem. Lett. 36 (2025) 110108.
[3] Z.C. Sun, M.S. Zhu, X.S. Lv, et al., Appl. Catal. B: Environ. 246 (2019) 330–336.
[4] X.L. Zhao, S. Chen, H.J. Yin, et al., Matter 3 (2020) 935–949.
[5] X. Ma, H. Liu, W.J. Yang, et al., J. Am. Chem. Soc. 143 (2021) 12220–12229.
[6] W. Zhou, Q.W. Deng, H.J. He, et al., Angew. Chem. Int. Ed. 62 (2023) e202214143.
[7] H.Y. Ma, Y. Liu, R. Xiong, J.H. Wei, Chin. Chem. Lett. 33 (2022) 1042–1046.
[8] W. Li, J.J. Li, Z.F. Liu, et al., Rare Met. 43 (2024) 533–542.
[9] X.W. Zhang, P. Wang, X.Y. Lv, et al., ACS Catal. 12 (2022) 2569–2580.
[10] D.Z. Kong, X.X. Ruan, J.K. Geng, et al., Int. J. Hydrogen Energ. 46 (2021) 28043–28052.
[11] Y.J. Wang, S.R. Kavanagh, I.B. Ceballos, et al., Nat. Photon. 16 (2022) 235–241.
[12] R.M. Jauhar, K. Ramachandran, S. Deepapriya, et al., Int. J. Hydro. Energy 77 (2024) 291–300.
[13] N. Akhtar, N. Nadeem, M. Yaseen, et al., Mater. Chem. Phys. 316 (2024) 129067.
[14] W. Li, J.J. Li, H.Y. Ma, et al., J. Colloid. Interface Sci. 657 (2024) 728–737.
[15] Y. Tang, J.H. Qiu, D.L. Dai, et al., Sep. Purif. Tech. 354 (2025) 129350.
[16] G.Z.S. Ling, S.H.W. Kok, P.P. Zhang, et al., Adv. Funct. Mater. 34 (2024) 2409320.
[17] T. Manimozhi, J. Archana, M. Navaneethan, K. Ramamurthi, Appl. Surf. Sci. 487 (2019) 664–673.
[18] A. Kolay, H. Flint, E.A. Gibson, M. Deepa, Chem. Eng. J. 437 (2022) 135223.
[19] X.H. Wang, X. H.Wang, J.F. Huang, et al., Nat. Commun. 12 (2021) 4112.
[20] P. Ganguly, S. Mathew, L. Clarizia, et al., Appl. Catal. B: Environ. 253 (2019) 401–418.
[21] F.Y. Xu, Y. He, J.J. Zhang, et al., Angew. Chem. Int. Ed. 63 (2024) e202414672.
[22] T. Jiang, Z.W. Wang, G. Wei, et al., ACS Energy Lett. 9 (2024) 1915–1922.
[23] Y.M. Feng, D.M. Chen, Y. Zhong, et al., ACS Appl. Mater. Interfaces 15 (2023) 9221–9230.
[24] A. Kumar, S.K. Sharma, G. Sharma, et al., J. Hazard. Mater. 364 (2019) 429–440.
[25] J.J. Li, Z. Liu, W. Li, et al., J. Colloid. Interface Sci. 682 (2025) 41–49.
[26] M.L. Gu, J.J. Zhang, I.V. Kurganskii, et al., Adv. Mater. 44 (2024) 2414803.
[27] J.H. Ma, L. Xu, Z.Y. Yin, et al., Appl. Catal. B: Environ. Energy 344 (2024) 123601.
[28] M.X. Tan, C.Y. Yu, H. Zeng, et al., Nanoscale 15 (2023) 2425–2434.
[29] W.J. Zhong, M.Y. Hung, Y.T. Kuo, et al., Adv. Mater. 44 (2024) 2403228.
[30] W.J. Su, Y.L. Zhang, A. Kuklin, et al., ACS Catal. 14 (2024) 13927–13939.
[31] H.R. Zhang, M.Y. Cui, Y.J. Lv, Y.F. Rao, Y. Huang, Chin. Chem. Lett. 36 (2025) 110108.
[32] S. Zhang, J. Sun, H. Ju, Small 20 (2024) 2405712.
[33] J.Q. Zhang, W.K. Ling, A.H. Li, et al., Adv. Funct. Mater. 34 (2024) 2405420.
[34] X.L. Zhang, F. Wu, G.C. Li, et al., Appl. Catal. B: Environ. 342 (2024) 123398.
[35] Q.Q. Zhang, Z. Wang, Y.H. Song, et al., J. Mater. Sci. Tech. 169 (2024) 148–157.
[36] T. Sun, C.X. Li, Y.P. Bao, J. Fan, E.Z. Liu, Acta Phys. Chim. Sin. 39 (2023) 2212009.

[37] Q.S. Zhang, S.Y. Yuan, H.B. Yin, Z.J. Guan, J. Mater. Chem. A 12 (2024) 18204.
[38] Y. Li, S. Yu, J. Xiang, et al., ACS Catal. 13 (2023) 8281–8292.
[39] Y.F. Zhang, Z.Y. Zhang, J. Mater. Sci. Tech. 171 (2023) 147–149.
[40] S. Wang, D. Zhang, X. Pu, et al., Small 20 (2024) 2311504.
[41] W. Li, G.C. Zuo, S.S. Ma, et al., Appl. Catal. B: Environ. Energ. 365 (2025) 124971.
[42] C.Y. Yang, Q.Y. Rong, F.Y. Shi, et al., Chin. Chem. Lett. 35 (2024) 109767.
[43] S.J. Li, C.J. You, F. Yang, et al., Chin. J. Catal. 68 (2025) 259–271.
[44] R.Q. Zhang, R.C. Liu, Z.H. Ding, et al., J. Colloid. Interface Sci. 682 (2025) 568–577.
[45] X.Y. Deng, J.J. Zhang, K.Z. Qi, et al., Nat. Commun. 15 (2024) 4807.
[46] Z.S. Kong, D.F. Zhang, J.C. Liu, et al., Nano Energy 138 (2025) 110890.